

# A VECTOR FINITE ELEMENT TIME-DOMAIN METHOD FOR SOLVING MAXWELL'S EQUATIONS ON UNSTRUCTURED HEXAHEDRAL GRIDS\*

GARRY RODRIGUE<sup>†</sup> AND DANIEL WHITE<sup>‡</sup>

**Abstract.** In this paper the vector finite element time-domain (VFETD) method is derived, analyzed, and validated. The VFETD method uses edge vector finite elements as a basis for the electric field and face vector finite elements as a basis for the magnetic flux density. The Galerkin method is used to convert Maxwell's equations to a coupled system of ordinary differential equations. The leapfrog method is used to advance the fields in time. The method is shown to be stable and to conserve energy and charge for arbitrary hexahedral grids. A numerical dispersion analysis shows the method to be second order accurate on distorted hexahedral grids. Several computational experiments are performed to determine the accuracy and efficiency of the method.

**Key words.** Maxwell's equations, vector finite element, unstructured grids, edge elements

**AMS subject classification.** 74S05

**PII.** S1064827598343826

**1. Introduction.** This paper is concerned with the numerical solution of the time dependent Maxwell equations in charge-free regions,

$$\begin{aligned} \frac{\partial \mathbf{B}}{\partial t} &= -\nabla \times \mathbf{E} - \sigma_M \mu^{-1} \mathbf{B}, \\ \varepsilon \frac{\partial \mathbf{E}}{\partial t} &= \nabla \times \mu^{-1} \mathbf{B} - \sigma_E \mathbf{E} - \mathbf{J}, \\ \nabla \cdot \varepsilon \mathbf{E} &= 0, \\ \nabla \cdot \mathbf{B} &= 0, \end{aligned} \tag{1}$$

with initial-boundary values

$$\hat{\mathbf{n}} \times \mathbf{E} = \mathbf{E}_{bc} \quad \text{on } \Gamma = \text{boundary } (\Omega), \tag{2}$$

$$\mathbf{E}(t=0) = \mathbf{E}_{ic}, \mathbf{B}(t=0) = \mathbf{B}_{ic}. \tag{3}$$

Here,  $\mathbf{E} = \mathbf{E}(x, t)$  is the electric field,  $\mathbf{B} = \mathbf{B}(x, t)$  is the magnetic flux density,  $\mathbf{J} = \mathbf{J}(x, t)$  is the electric current, and  $\hat{\mathbf{n}}$  is the outward normal vector to  $\Gamma$ . The volume  $\Omega \subset R^3$  is a domain, not necessarily bounded, whose boundary  $\Gamma$  is sufficiently regular (Lipschitz-continuous).  $\Omega$  may be inhomogeneous, consisting of several dielectric, magnetic, and metallic regions of arbitrary geometry. The material properties are assumed to be linear and nondispersive. The volume may also contain several independent voltage and current sources. The electric and magnetic conductivities,  $\sigma_E$

\*Received by the editors August 24, 1998; accepted for publication (in revised form) March 5, 2001; published electronically August 15, 2001. This research was supported under the auspices of the U.S. Department of Energy by Lawrence Livermore National Laboratory contract W-7405-Eng-48.

<http://www.siam.org/journals/sisc/23-3/34382.html>

<sup>†</sup>Department of Applied Science, University of California at Davis, CA, and Lawrence Livermore National Laboratory, P.O. Box 808, L-561, Livermore, CA 94551 (ghrodrigue@ucdavis.edu).

<sup>‡</sup>Center for Applied Scientific Computing, Lawrence Livermore National Laboratory, P.O. Box 808, L-561, Livermore, CA 94551 (dwhite@llnl.gov).

and  $\sigma_M$ , the dielectric permittivity  $\varepsilon$ , and the magnetic permeability  $\mu$  are assumed to be time independent symmetric positive definite tensors. Example electromagnetic problems within this class include the design of waveguides and antennas, scattering of electromagnetic waves from automobiles and aircraft, and the penetration and absorption of electromagnetic waves by dielectric objects. Throughout this presentation, unless the physical meaning of quantities suggests otherwise, boldface letters will stand for vector fields whereas plain faced letters will stand for scalar fields.

The most popular numerical scheme for solving the time dependent Maxwell equations on an orthogonal Cartesian grid is the finite difference time-domain (FDTD) method [1, 2, 3, 4]. The method utilizes a centered difference approximation in space and a leapfrog approximation in time to yield a conditionally stable, consistent, and second order accurate scheme. However, when one attempts to use the FDTD method on complicated geometries by approximating curved boundaries with “stair steps,” poor results are obtained [4, 5]. Nevertheless the FDTD method is extremely efficient and is the benchmark to which new methods are compared.

There have been several attempts to generalize the FDTD method to unstructured hexahedral grids, most notably the modified finite volume (MFV) and discrete surface integral (DSI) methods [6, 7, 8, 9]. In these methods Maxwell’s equations are cast in integral form, then the subsequent volume and/or surface integrals are approximated by standard integration rules. A leap frog time integration is used so that these methods reduce to the FDTD method when orthogonal grids are used. However, the finite volume methods are not provably stable, and weak instabilities leading to nonphysical solution growth have been observed for nonorthogonal grids [10]. The instability is caused by the nonsymmetric discretization of the curl-curl operator. Dissipative time integration schemes may be employed to counteract this nonphysical solution growth, but this results in a violation of conservation of energy [11].

There is another class of finite volume methods where Maxwell’s curl equations are cast in conservative form, resulting in a PDE that resembles the Euler equation of fluid dynamics [12, 13, 14]. The classical methods of computational fluid dynamics such as Lax–Wendroff or Godunov can then be used to solve the equations. These methods can be implemented on a structured, but nonorthogonal, hexahedral grid but do not reduce to the FDTD method when implemented on orthogonal Cartesian grids. However, these methods are stable and consistent, and very good accuracy can be achieved as the grid is refined. The methods rely upon dissipative time integration for stability and consequently do not conserve energy. In addition they neglect the divergence properties of the fields so that there is no guarantee that these methods will conserve charge.

Vector finite elements, also known as edge elements, Whitney 1-forms, or  $H(\text{curl})$  elements [15, 16, 17, 18, 19], have been used to formulate finite element solutions to the weak form of Maxwell’s equations. These elements enforce tangential continuity of the fields but allow for jump discontinuity in the normal component of the fields. Use of these elements also eliminates spurious, divergent solutions of Maxwell’s equations that were common with nodal element formulations [20, 21, 22, 23, 24, 25]. Vector finite element methods have been successfully used in the frequency domain to analyze resonant cavities, compute waveguide modes, and perform scattering calculations [26, 27, 28]. Vector finite elements have also been proposed to solve Maxwell’s equations directly in the time domain [29, 30, 31, 32, 33]. Theoretical convergence results and error estimates for time dependent vector finite element solutions of Maxwell’s equations were developed in [34, 35].

**1.1. Vector finite element time-domain (VFETD) method.** In this paper, a Galerkin procedure is used to convert the weak form of Maxwell's equations to a semidiscrete coupled system of ordinary differential equations using vector finite elements. A leapfrog time integration scheme similar to that found in the FDTD method is then used to discretize time and update the field variables.

The VFETD method uses vector "edge" finite elements as a basis for the electric field and vector "face" finite elements as a basis for the magnetic flux density. These elements are complementary in the sense that the edge elements have tangential continuity across interfaces whereas the face elements have normal continuity across interfaces. Consequently, the Galerkin approximations preserve field continuities/discontinuities across material interfaces. The properties of these vector finite elements is discussed in detail in [15].

The VFETD method is shown to be conditionally stable. Moreover, if a stable time step is used, the method conserves energy and charge, independent of how distorted the grid is. A numerical dispersion analysis of the method is performed on several different distorted hexahedral grids, with the result that the method is second order accurate. The analysis also shows how the anisotropic part of the numerical dispersion relation depends upon the grid distortion [40, 41, 42, 43].

The VFETD method requires a sparse linear system to be solved at every time step. The computational effort required to solve the system depends upon how distorted the grid is. For Cartesian grids mass lumping can be used, in which case the VFETD method reduces to the classic FDTD method. For non-Cartesian grids conjugate gradient iterative methods are used to solve the system where it is shown, via computational experiments on unstructured hexahedral grids, that the number of iterations required to achieve a given accuracy is a constant independent of the grid cell size (grid refinement) used to discretize the problem. Hence the method is scalable. The accuracy of the method, as well as the required CPU time, are tabulated for resonant cavity, waveguide, and antenna problems.

**2. Weak formulation of Maxwell's equations.** In this section we convert Maxwell's equations into variational equations posed over suitable function spaces. We first consider the space

$$H(\text{curl}; \Omega) = \{\mathbf{u} \in \mathbf{L}_2(\Omega); \nabla \times \mathbf{u} \in \mathbf{L}_2(\Omega)\}.$$

A function  $\mathbf{u}$  in the vector space  $\mathbf{H}^1(K_1) \cup \mathbf{H}^1(K_2)$  is in  $H(\text{curl}; \Omega = K_1 \cup K_2)$  if and only if the trace  $\mathbf{u} \times \mathbf{n}$  is the same on each side of the face  $\Gamma$  [15, 16]. Consequently,  $H(\text{curl}; \Omega)$  is an appropriate space for the electric field  $\mathbf{E}$ . Similarly, we define the function space

$$H(\text{div}; \Omega) = \{\mathbf{u} \in \mathbf{L}_2(\Omega); \nabla \bullet \mathbf{u} \in L_2(\Omega)\}.$$

Then, a function  $\mathbf{u}$  in the vector space  $\mathbf{H}^1(K_1) \cup \mathbf{H}^1(K_2)$  is in  $H(\text{div}; \Omega = K_1 \cup K_2)$  if and only if  $\mathbf{u} \bullet \mathbf{n}$  is the same on each side of the face  $\Gamma$  [15, 16]. Hence,  $H(\text{div}; \Omega)$  is an appropriate space to which the magnetic flux density  $\mathbf{B}$  should belong. Both spaces, equipped with the canonical inner products, are Hilbert spaces with norms

$$\begin{aligned} \|\mathbf{u}\|_{H(\text{curl}; \Omega)} &= (\|\mathbf{u}\|_2^2 + \|\nabla \times \mathbf{u}\|_2^2)^{1/2}, \\ \|\mathbf{u}\|_{H(\text{div}; \Omega)} &= (\|\mathbf{u}\|_2^2 + \|\nabla \bullet \mathbf{u}\|_2^2)^{1/2}. \end{aligned}$$

We write  $\|\mathbf{u}\|_2^2 = \int_{\Omega} \mathbf{u}^t \mathbf{u} d\Omega \equiv (\mathbf{u}, \mathbf{u}) < \infty$  for the  $\mathbf{L}_2(\Omega)$ -norm and  $(\mathbf{u}, \mathbf{v}) = \int_{\Omega} \mathbf{u}^t \mathbf{v} d\Omega$  for the  $\mathbf{L}_2(\Omega)$  inner product. The subspace of  $H(\text{curl}; \Omega)$  containing the vector fields

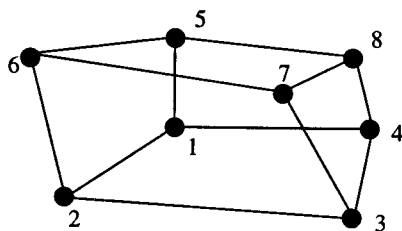


FIG. 1. Illustration of an arbitrary hexahedron.

$\mathbf{u}$  with vanishing tangential trace  $\mathbf{n} \times \mathbf{u}$  on  $\Gamma$  is denoted by  $H_0(\text{curl}; \Omega)$ . As usual,  $\mathbf{n}$  designates the exterior unit normal vector on  $\Gamma$ . Similarly,  $H_0(\text{div}; \Omega)$  denotes the subspace of  $H(\text{div}; \Omega)$  containing vectors  $\mathbf{u}$  such that  $\mathbf{u} \cdot \mathbf{n} = 0$  on  $\Gamma$ .

Given the above definitions, a natural way of defining the weak form of Maxwell's equations (1)–(3) is to determine functions  $\mathbf{B} \in H(\text{div}; \Omega)$ ,  $\mathbf{E} \in H(\text{curl}; \Omega)$  such that

$$(4) \quad \frac{\partial}{\partial t}(\mu^{-1} \mathbf{B}, \mathbf{B}^*) = -(\mu^{-1} \nabla \times \mathbf{E}, \mathbf{B}^*) = (\mu^{-1} \sigma_M \mu^{-1} \mathbf{B}, \mathbf{B}^*),$$

$$(5) \quad \frac{\partial}{\partial t}(\varepsilon \mathbf{E}, \mathbf{E}^*) = (\nabla \times \mathbf{E}^*, \mu^{-1} \mathbf{B}) - (\sigma_E \mathbf{E}, \mathbf{E}^*) - (J, \mathbf{E}^*)$$

for all  $\mathbf{B}^* \in H_0(\text{div}; \Omega)$ ,  $\mathbf{E}^* \in H_0(\text{curl}; \Omega)$ . The multiplication of the first equation by  $\mu^{-1}$  is done to aid in the analysis of the Galerkin method. Clearly, if  $\mathbf{B}$ ,  $\mathbf{E}$  are classical solutions of Maxwell's equations (1)–(3), then they are solutions of the weak equations (4)–(5).

**3. Finite element basis functions.** A general definition of finite elements on arbitrary polyhedra is given by the following.

DEFINITION. A finite element  $(K, P, A)$ , consists of

1.  $K$ , a polyhedral domain;
2.  $P$ , a vector space of polynomials defined on  $K$  having a basis  $\{\psi_1, \psi_2, \dots, \psi_N\}$  (called shape functions);
3.  $A$ , a set of linear functionals defined on  $P$  having a basis  $\alpha_1, \alpha_2, \dots, \alpha_N$  (called the degrees of freedom).

In this section we define  $K, P, A$  for the linear edge and face elements. For the elements developed in this paper, we shall approximate the domain  $\Omega$  with a hexahedral mesh  $\kappa$  consisting of  $K_i, i = 1, \dots, N$ , hexahedra. Each of the hexahedra can be mapped using the standard trilinear mapping  $(x, y, z) = B(\zeta, \eta, \nu)$  to a reference element,  $K_0 = \{0 \leq \zeta, \eta, \nu \leq 1\}$ . We require that the mapping  $B$  be one-to-one and invertible, implying a nonsingular Jacobian matrix  $J$ . Consequently,  $K$  will be a hexahedron consisting of 8 nodes labeled as in Figure 1. The 12 edges,  $a_i$ , and 6 faces,  $f_i$ , are numbered according to Table 1. The Dirichlet part of the boundary  $\Gamma_D$  is assumed to be the union of complete faces of elements.

**3.1. Finite elements in  $H(\text{curl})$ : Edge elements.** We consider finite elements  $(K, P, A)$ , called “edge elements,” where  $K$  is an arbitrary hexahedron and the degrees of freedom of  $A$  are defined by

$$(6) \quad \alpha_i(v) = \int_{a_i} (v \cdot \mathbf{t}_i) ds, v \in P$$

TABLE 1  
Node, edge, and face numbering scheme for hexahedrons.

| $i$ | edge, $a_i$ | face, $f_i$ |
|-----|-------------|-------------|
| 1   | 1-2         | 1-4-8-5     |
| 2   | 4-3         | 2-3-7-6     |
| 3   | 5-6         | 1-5-6-2     |
| 4   | 8-7         | 4-8-7-3     |
| 5   | 1-4         | 1-2-3-4     |
| 6   | 5-8         | 5-6-7-8     |
| 7   | 2-3         |             |
| 8   | 6-7         |             |
| 9   | 1-5         |             |
| 10  | 2-6         |             |
| 11  | 4-8         |             |
| 12  | 3-7         |             |

with  $\mathbf{t}_i$  being the unit tangent vector along edge  $a_i$  of  $K$ . The space  $P$  is defined by considering the reference element  $(K_0, P_0, A_0)$ . Here

$$P_0 = \{\mathbf{u} = [u_1, u_2, u_3]^t : u_1 \in Q_{0,1,1}; u_2 \in Q_{1,0,1}; u_3 \in Q_{1,1,0}\},$$

where  $Q_{l,m,n}$  denotes the vector space of polynomials in three variables  $(x, y, z)$ , the maximum degree of which are, respectively,  $l$  in  $x$ ,  $m$  in  $y$ ,  $n$  in  $z$ . Note that *dimension*  $[P_0] = 12$ . The basis for  $P_0$ , as constructed by (6), is

$$\begin{aligned}
 \mathbf{W}_1^{(0)} &= (1 - y - z + yz, 0, 0), & \mathbf{W}_2^{(0)} &= (y - yz, 0, 0), \\
 \mathbf{W}_3^{(0)} &= (z - yz, 0, 0), & \mathbf{W}_4^{(0)} &= (yz, 0, 0), \\
 \mathbf{W}_5^{(0)} &= (0, 1 - x - z - xz, 0), & \mathbf{W}_6^{(0)} &= (0, x - xz, 0), \\
 \mathbf{W}_7^{(0)} &= (0, z - xz, 0), & \mathbf{W}_8^{(0)} &= (0, xz, 0), \\
 \mathbf{W}_9^{(0)} &= (0, 0, 1 - x - y - xy), & \mathbf{W}_{10}^{(0)} &= (0, 0, x - xy), \\
 \mathbf{W}_{11}^{(0)} &= (0, 0, y - xy), & \mathbf{W}_{12}^{(0)} &= (0, 0, xy).
 \end{aligned}
 \tag{7}$$

The above polynomial basis defined on the reference element must be transformed to the arbitrary hexahedron  $K$  such that the degrees of freedom are preserved. It is well known that the covariant transformation preserves line integrals under a change of coordinates; hence we define  $P$  in  $(K, P, A)$  by  $\mathbf{W}_i = J^{-t} \mathbf{W}_i^{(0)}$ .

**3.2. Finite elements in  $H(\text{div})$ : Face elements.** We now consider a finite element  $(K, P, A)$ , called “face elements,” where  $K$  is an arbitrary hexahedron and the degrees of freedom of a face element are

$$\alpha_i(v) = \int_{f_i} (v \bullet \mathbf{n}_i) ds,
 \tag{8}$$

where  $\mathbf{n}_i$  is the unit normal vector to the face  $f_i$  of  $K$ . The space  $P$  is defined by again considering the reference element  $(K_0, P_0, A_0)$ . Here,  $P_0 = \{\mathbf{u} = [u_1, u_2, u_3]^t :$

$u_1 \in Q_{1,0,0}$ ;  $u_2 \in Q_{0,1,0}$ ;  $u_3 \in Q_{0,0,1}$ . The basis functions of  $P_0$  are constructed from (8) to get

$$(9) \quad \begin{aligned} \mathbf{F}_1^{(0)} &= (-1+x, 0, 0), & \mathbf{F}_2^{(0)} &= (x, 0, 0), & \mathbf{F}_3^{(0)} &= (0, -1+y, 0), \\ \mathbf{F}_4^{(0)} &= (0, y, 0), & \mathbf{F}_5^{(0)} &= (0, 0, -1+z), & \mathbf{F}_6^{(0)} &= (0, 0, z). \end{aligned}$$

The above polynomial basis defined on the reference element must be transformed to the arbitrary hexahedron  $K$  such that the degrees of freedom are preserved. It is well known that a contravariant transformation preserves surface integrals; hence we define  $P$  in  $(K, P, A)$  by  $\mathbf{F}_i = J\mathbf{F}_i^{(0)}$ .

**4. Galerkin approximation of Maxwell's equations.** The Galerkin method constructs approximations

$$(10) \quad \begin{aligned} \tilde{\mathbf{E}} &= \sum_{j=1}^{N_E} e_j \mathbf{W}_j \in W = \text{span} [\mathbf{W}_1, \mathbf{W}_2, \dots, \mathbf{W}_{N_E}] \subset H_0(\text{curl}; \Omega), \\ \tilde{\mathbf{B}} &= \sum_{j=1}^{N_B} b_j \mathbf{F}_j \in F = \text{span} [\mathbf{F}_1, \mathbf{F}_2, \dots, \mathbf{F}_{N_E}] \subset H_0(\text{div}; \Omega), \end{aligned}$$

such that

$$(11) \quad \begin{aligned} \frac{\partial}{\partial t}(\mu^{-1}\tilde{\mathbf{B}}, \mathbf{F}_i) &= -(\mu^{-1}\nabla \times \tilde{\mathbf{E}}, \mathbf{F}_i) + -(\mu^{-1}\sigma_M\mu^{-1}\tilde{\mathbf{E}}, \mathbf{F}_i), & i &= 1, 2, \dots, N_F, \\ \frac{\partial}{\partial t}(\varepsilon\tilde{\mathbf{E}}, \mathbf{W}_i) &= (\nabla \times \mathbf{W}_i, \mu^{-1}\tilde{\mathbf{E}}) - (\sigma_E\tilde{\mathbf{B}}, \mathbf{W}_i) - (\mathbf{j}, \mathbf{W}_i), & i &= 1, 2, \dots, N_E, \end{aligned}$$

where  $N_E$  and  $N_F$  are the number of internal edges and faces, respectively. This leads to systems of ordinary differential equations

$$(12) \quad \begin{aligned} G \frac{\partial \mathbf{b}}{\partial t} &= -K\mathbf{e} - P\mathbf{b}, \\ C \frac{\partial \mathbf{e}}{\partial t} &= K^T\mathbf{b} - S\mathbf{e} - Q\mathbf{j}, \end{aligned}$$

where  $\mathbf{b} = [b_1, b_2, \dots, b_{N_F}]^t$ ,  $\mathbf{e} = [e_1, e_2, \dots, e_{N_E}]^t$ , and the matrices are given by

$$(13) \quad \begin{aligned} G_{ij} &= (\mu^{-1}\mathbf{F}_i, \mathbf{F}_j), & K_{ij} &= (\mu^{-1}\nabla \times \mathbf{W}_i, \mathbf{F}_j), \\ P_{ij} &= (\mu^{-1}\sigma_M\mu^{-1}\mathbf{F}_i, \mathbf{F}_j), & C_{ij} &= (\varepsilon\mathbf{W}_i, \mathbf{W}_j), \\ K_{ij}^t &= (\mu^{-1}\nabla \times \mathbf{W}_j, \mathbf{F}_i), & S_{ij} &= (\sigma_E\mathbf{W}_i, \mathbf{W}_j), & Q_{ij} &= (\mathbf{F}_i, \mathbf{W}_j). \end{aligned}$$

**5. Leapfrog time differencing.** The ordinary differential equations (12) are differenced so that the electric fields are calculated at whole time steps and the magnetic fields are calculated at the half time steps. Specifically,

$$(14) \quad (G + \Delta t P/2)\mathbf{b}^{n+1/2} = -\Delta t K\mathbf{e}^n + (G - \Delta t P/2)\mathbf{b}^{n-1/2},$$

$$(15) \quad (C + \Delta t S/2)\mathbf{e}^{n+1} = \Delta t K^T\mathbf{b}^{n+1/2} + (C - \Delta t S/2)\mathbf{e}^n - \Delta t Q\mathbf{j}^{n+1/2}.$$

**5.1. Stability and conservation.** Properties of (14) will be derived by assuming no electric or magnetic conductivity, i.e.,  $\sigma_E = \sigma_M = \mathbf{J} = 0$ . In this case the discrete equations (14) become

$$(16) \quad \begin{bmatrix} \mathbf{e}^{n+1} \\ \mathbf{b}^{n+1/2} \end{bmatrix} = \begin{bmatrix} (I - \Delta t^2 C^{-1} K^t G^{-1} K) & \Delta t C^{-1} K^t \\ -\Delta t G^{-1} K & I \end{bmatrix} \begin{bmatrix} \mathbf{e}^n \\ \mathbf{b}^{n-1/2} \end{bmatrix}.$$

The following theorem establishes eigenproperties of the method.

**THEOREM 1.** *Let  $T(\Delta t)$  be the amplification matrix in (16). Then*

- (a) *the eigenvalues of  $T(\Delta t)$  either have unit magnitude or are negative*
- (b) *the eigenvalues of  $T(\Delta t)$  have unit magnitude if and only if*

$$(17) \quad \Delta t \leq \frac{2}{\sqrt{\max(\psi)}},$$

where  $\psi$  is an eigenvalue of  $C^{-1} K^t G^{-1} K$ .

*Proof.* (a) Suppose  $T(\Delta t)$  has a complex eigenvalue  $\lambda = a + ib$ . Then there is a complex eigenvector  $\begin{bmatrix} x \\ y \end{bmatrix}$  that solves the eigenvalue problem

$$\begin{bmatrix} (I - \Delta t^2 C^{-1} K^t G^{-1} K) & \Delta t C^{-1} K^t \\ -\Delta t G^{-1} K & I \end{bmatrix} \begin{bmatrix} \mathbf{x} \\ \mathbf{y} \end{bmatrix} = \lambda \begin{bmatrix} \mathbf{x} \\ \mathbf{y} \end{bmatrix}.$$

Since the matrices  $C$  and  $G$  are symmetric and positive definite, they admit Cholesky decompositions  $C = \tilde{C}^t \tilde{C}$  and  $G = \tilde{G}^t \tilde{G}$ , respectively. If we let  $\tilde{\mathbf{x}} = \tilde{C} \mathbf{x}$  and  $\tilde{\mathbf{y}} = \tilde{G} \mathbf{y}$ , then the above eigenproblem is equivalent to

$$(18) \quad \begin{bmatrix} (I - \Delta t^2 Q Q^t) & \Delta t Q \\ -\Delta t Q^t & I \end{bmatrix} \begin{bmatrix} \tilde{\mathbf{x}} \\ \tilde{\mathbf{y}} \end{bmatrix} = \lambda \begin{bmatrix} \tilde{\mathbf{x}} \\ \tilde{\mathbf{y}} \end{bmatrix},$$

where the matrix  $Q$  is given by  $Q = \tilde{C}^{-t} K^t \tilde{G}^{-1}$ . Note that  $Q Q^t = C^{-1} K^t G^{-1} K$ . Since

$$\begin{bmatrix} (I - \Delta t^2 Q Q^t) & \Delta t Q \\ -\Delta t Q^t & I \end{bmatrix} = \begin{bmatrix} I & \Delta t Q \\ O & I \end{bmatrix} \begin{bmatrix} I & O \\ -\Delta t Q^t & I \end{bmatrix},$$

its determinant is 1 and consequently  $\lambda \neq 0$ . We can now write (18) as a general eigenproblem:

$$\begin{bmatrix} I & O \\ -\Delta t Q^t & I \end{bmatrix} \begin{bmatrix} \tilde{\mathbf{x}} \\ \tilde{\mathbf{y}} \end{bmatrix} = \lambda \begin{bmatrix} I & \Delta t Q \\ O & I \end{bmatrix}^{-1} \begin{bmatrix} \tilde{\mathbf{x}} \\ \tilde{\mathbf{y}} \end{bmatrix} = \lambda \begin{bmatrix} I & -\Delta t Q \\ O & I \end{bmatrix} \begin{bmatrix} \tilde{\mathbf{x}} \\ \tilde{\mathbf{y}} \end{bmatrix}.$$

We get that

$$(1 - \lambda) \tilde{\mathbf{y}} = \Delta t Q^t \tilde{\mathbf{x}}$$

and

$$-\lambda \Delta t^2 Q Q^t \tilde{\mathbf{x}} = (1 - \lambda)^2 \tilde{\mathbf{x}}.$$

Hence,  $\tilde{\mathbf{x}}$  is an eigenvector of  $Q Q^t$  with eigenvalue  $-(\lambda - 1)^2 / \lambda \Delta t^2$ . Since  $Q Q^t$  is symmetric, it has only real eigenvalues. Thus,

$$\operatorname{Im} \left( \frac{-(\lambda - 1)^2}{\lambda} \right) = \operatorname{Im} \left( 2 - \frac{(\lambda^2 + 1)}{\lambda} \right) = \operatorname{Im}(\lambda + \lambda^{-1}) = b(1 - (a^2 + b^2)^{-1}) = 0.$$

It follows that either  $b = 0$ , in which case  $\lambda$  is real, or  $|\lambda| = 1$ . If  $\lambda$  is real, then using the fact that  $QQ^t$  is positive semidefinite we see its eigenvalues are nonnegative so that  $\lambda = 1$  or  $\lambda < 0$ .

(b) Now suppose that condition (17) holds. In view of (a), we need only consider the case  $\lambda < 0$ . Then

$$\Delta t^2 \leq \frac{4}{\psi} \leq \frac{-4\lambda\Delta t^2}{(\lambda-1)^2} \Rightarrow (\lambda+1)^2 \leq 0 \Rightarrow \lambda = -1.$$

Now suppose all eigenvalues of  $T(\Delta t)$  have unit magnitude. Let  $\psi = (2+\alpha)/\Delta t^2$  be the eigenvalue of  $QQ^t$  that is largest in magnitude. Let  $\lambda$  be such that  $\alpha = -(\lambda^2 + 1)/\lambda$ . Specifically,  $\lambda$  is given by

$$\lambda = \frac{-\alpha \pm \sqrt{\alpha^2 - 4}}{2}.$$

Moreover, using the same arguments as in (a) to show the connection between the eigenvalues of  $QQ^t$  and  $T(\Delta t)$ , we see that  $\lambda$  is an eigenvalue of  $T(\Delta t)$  and by hypothesis has unit magnitude. Then

$$\frac{\Delta t^2}{4} |\psi| = \frac{|\lambda-1|^2}{4|\lambda|} \leq 1$$

and the theorem is proved.  $\square$

**THEOREM 2** (conservation of magnetic charge). *If  $\tilde{\mathbf{B}}^{n+1/2} = \sum_{i=1}^{N_f} b_i^{n+1/2} \mathbf{F}_i$  is the Galerkin approximation computed from (16), then*

$$\int_{\Omega} \nabla \bullet \tilde{\mathbf{B}}^{n+1/2} d\Omega = \int_{\Omega} \nabla \bullet \tilde{\mathbf{B}}^{n-1/2} d\Omega, \quad n = 1, 2, \dots$$

*Proof.* Let  $\delta \mathbf{b}^n = (\mathbf{b}^{n+1/2} - \mathbf{b}^{n-1/2})/\Delta t$ . Then by (16)

$$G\delta \mathbf{b}^n = -K\mathbf{e}^n.$$

Note that the edge basis functions and the face basis functions are related by the so-called inclusion (or compatibility) condition  $\nabla \times \mathbf{W}_i \in F$ . In particular, the edge and face basis functions are normalized such that  $\nabla \times W_i = \sum_{j=1}^2 a_{ij} \mathbf{F}_{ij}$ , where  $\mathbf{F}_{ij}$  are the two face functions associated with the edge function  $W_i$  and  $a_{ij} = \pm 1$  with the sign depending upon the right-hand rule. Thus,

$$\sum_{i=1}^{N_e} e_i \nabla \times \mathbf{W}_i = \sum_{i=1}^{N_e} e_i \sum_{j=1}^2 a_{ij} \mathbf{F}_{ij}$$

and by (16) we have

$$\sum_{i=1}^{N_f} \delta b_i^n (\mathbf{F}_i, \mathbf{F}_k) = \sum_{i=1}^{N_e} e_i^n (\nabla \times \mathbf{W}_i, \mathbf{F}_k) = \sum_{i=1}^{N_e} e_i^n \sum_{j=1}^2 a_{ij} (\mathbf{F}_{ij}, \mathbf{F}_k)$$

for  $k = 1, \dots, N_f$ . The two summations in the right-hand term can be combined so that the summation is performed over all  $N_f$  face, with four electric field degrees of freedom  $e_j$  contributing to each  $b_i$ :

$$\sum_{i=1}^{N_f} \delta b_i^n (\mathbf{F}_i, \mathbf{F}_k) = \sum_{i=1}^{N_f} \left( \sum_{j=1}^4 e_j^n a_{ij} \right) (\mathbf{F}_i, \mathbf{F}_k).$$



It follows that

$$\delta b_i^n = \sum_{j=1}^4 e_j^n a_{ij}$$

Using Gauss' law, the divergence of the magnetic flux density in a given cell  $\Omega_e$  is

$$\int_{\Omega} (\nabla \bullet \delta \tilde{\mathbf{B}}^n) = \oint \delta \tilde{\mathbf{B}}^n \bullet \mathbf{n} d\Gamma = \sum_{i=1}^6 \delta b_i^n = \sum_{i=1}^6 \sum_{j=1}^4 e_j^n a_{ij} = 0,$$

and the theorem follows by summing over the cells.  $\square$

**THEOREM 3** (conservation of electric charge). *Let  $S_0$  be the space of trilinear continuous Lagrangian finite elements vanishing on  $\gamma_D$ . If  $\tilde{\mathbf{E}}^n = \sum_{i=1}^{N_e} e_i^n \mathbf{W}_i$  is the Galerkin approximation computed from (16), then*

$$(19) \quad \int_{\Omega} (\nabla \bullet \varepsilon \tilde{\mathbf{E}}^n) \psi d\Omega = \int_{\Omega} (\nabla \bullet \varepsilon \tilde{\mathbf{E}}^{n-1}) \psi d\Omega, \quad n = 1, 2, \dots,$$

for all continuous piecewise linear functions  $\phi \in S_0$ .

*Proof.* First note that integration by parts yields

$$\int_{\Omega} (\nabla \bullet \varepsilon \tilde{\mathbf{E}}) \phi = - \int_{\Omega} \varepsilon \tilde{\mathbf{E}} \bullet \nabla \phi d\Omega + \oint_{\Gamma} \phi \varepsilon \tilde{\mathbf{E}} \bullet \mathbf{n} d\Gamma = - \int_{\Omega} \varepsilon \tilde{\mathbf{E}} \bullet \nabla \phi d\Omega.$$

Let  $\delta \tilde{\mathbf{E}}^n = \Delta t^{-1}(\tilde{\mathbf{E}}^n - \tilde{\mathbf{E}}^{n-1})$ . Then by (16),

$$(\varepsilon \delta \tilde{\mathbf{E}}^n, \mathbf{W}_j) = (\nabla \times \mathbf{W}_j, \mu^{-1} \tilde{\mathbf{B}}^{n-1/2}), \quad j = 1, 2, \dots, N_E.$$

Now,  $\nabla \phi \in W$ ; cf. [15, 25]. Therefore

$$\int_{\Omega} (\nabla \bullet \varepsilon \delta \tilde{\mathbf{E}}^n) \phi = \int_{\Omega} \varepsilon \delta \tilde{\mathbf{E}}^n \bullet \nabla \phi d\Omega = \int_{\Omega} (\nabla \times \nabla \phi) \bullet \mu^{-1} \tilde{\mathbf{B}}^{n-1/2} d\Omega = 0,$$

and the theorem is proved.  $\square$

**5.2. Numerical dispersion.** Equation (1) in an infinite, source free, zero conductivity region becomes the vector wave equation

$$(20) \quad \varepsilon \frac{\partial^2 \mathbf{E}}{\partial t^2} = -\nabla \times \mu^{-1} \nabla \times \mathbf{E}.$$

If  $\mu$  and  $\varepsilon$  are constant scalars, then

$$(21) \quad \mathbf{E} = \mathbf{E}_0 e^{I(\mathbf{k} \bullet \mathbf{x} - \omega t)}$$

is a solution to (20) only if the dispersion relation  $\omega^2 = c^2 k^2$  holds where  $k = \|\mathbf{k}\|_2$  and  $c = 1/(\sqrt{\mu\varepsilon})$  is the speed of light. Now, consider the solution

$$\mathbf{e}(t) = \sum_i e_i(t) \mathbf{W}_i(\mathbf{x}), \quad e_i(t) = \int_{a_i} \mathbf{E}(x, t) \bullet \mathbf{t} dl$$

of the Galerkin form of (20)

$$(22) \quad C \frac{\partial^2 \mathbf{e}}{\partial t^2} = -A \mathbf{e}, \quad e_i(0) = \int_{a_i} \mathbf{E}(\mathbf{x}, 0) \bullet \mathbf{t} dl$$

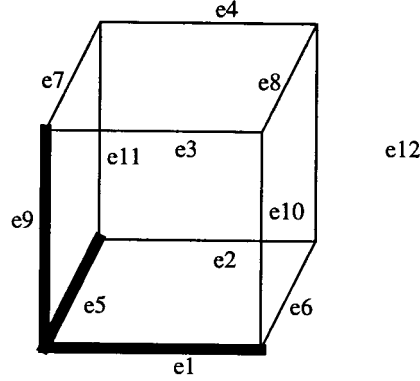


FIG. 2. Edge numbering for numerical dispersion analysis.

with  $\mathbf{t}$  the unit tangent vector to edge  $a_i$ . The matrices  $C$  and  $A$  are defined by (13) and  $A_{ij} = (\mu^{-1} \nabla \times \mathbf{W}_i, \nabla \times \mathbf{W}_j)$ , respectively. We now assume the grid to be composed of identical hexahedral cells, which may be distorted. For this analysis the distortion is such that edges  $\tilde{e}_1 - \tilde{e}_4$ ,  $\tilde{e}_5 - \tilde{e}_8$ ,  $\tilde{e}_9 - \tilde{e}_{12}$  are parallel; see Figure 2.

If we let

$$X(t) = \int_{\tilde{e}_1} \mathbf{E}(x, t) \bullet \mathbf{t} \, dl, \quad Y(t) = \int_{\tilde{e}_5} \mathbf{E}(x, t) \bullet \mathbf{t} \, dl, \quad Z(t) = \int_{\tilde{e}_9} \mathbf{E}(x, t) \bullet \mathbf{t} \, dl,$$

then

$$\begin{aligned} \tilde{e}_1(t) &= X(t), & \tilde{e}_2(t) &= X e^{I(\mathbf{k} \bullet \vec{\Delta}_{1,2} - \omega \Delta t)}, & \tilde{e}_3(t) &= X e^{I(\mathbf{k} \bullet \vec{\Delta}_{1,3} - \omega \Delta t)}, \\ \tilde{e}_4(t) &= X e^{I(\mathbf{k} \bullet \vec{\Delta}_{1,4} - \omega \Delta t)}, & \tilde{e}_5(t) &= Y(t), & \tilde{e}_6(t) &= Y e^{I(\mathbf{k} \bullet \vec{\Delta}_{5,6} - \omega \Delta t)}, \\ \tilde{e}_7(t) &= X e^{I(\mathbf{k} \bullet \vec{\Delta}_{5,7} - \omega \Delta t)}, & \tilde{e}_8(t) &= X e^{I(\mathbf{k} \bullet \vec{\Delta}_{5,8} - \omega \Delta t)}, & \tilde{e}_9(t) &= Z(t), \\ \tilde{e}_{10}(t) &= Z e^{I(\mathbf{k} \bullet \vec{\Delta}_{9,10} - \omega \Delta t)}, & \tilde{e}_{11}(t) &= Z e^{I(\mathbf{k} \bullet \vec{\Delta}_{9,11} - \omega \Delta t)}, & \tilde{e}_{12}(t) &= Z e^{I(\mathbf{k} \bullet \vec{\Delta}_{9,12} - \omega \Delta t)}, \end{aligned} \quad (23)$$

where  $\vec{\Delta}_{i,j}$  is the vector from the midpoint of edge  $\tilde{e}_i$  to the midpoint of edge  $\tilde{e}_j$ .

Clearly,

$$(24) \quad \left( \frac{\partial^2 \tilde{e}_i}{\partial t^2} \right)^n \approx \frac{\tilde{e}_i^{n+1} - 2\tilde{e}_i^n + \tilde{e}_i^{n-1}}{\Delta t^2} = \frac{\psi \tilde{e}_i}{\Delta t^2}, \quad \psi = 2 \cos(\omega \Delta t - 1).$$

If we assume  $\|\vec{\Delta}_{i,j}\|_2 = \Delta x$  for all  $(i, j)$ , then (22)–(24) yields a homogeneous system of equations:

$$(25) \quad (\psi F + \eta G) \begin{pmatrix} X \\ Y \\ Z \end{pmatrix} = 0, \quad \eta = c^2 \frac{\Delta t^2}{\Delta x^2}.$$

The numerical dispersion relation is given by

$$(26) \quad \det(\psi F + \eta G) = 0,$$

where the  $3 \times 3$  matrices  $F$ ,  $G$  are complicated nonlinear relationship between the wave vector  $\mathbf{k}$  and the radian frequency  $\omega$ . There are three roots; one is zero, which does not represent anything physical, and the other two correspond to the two distinct polarizations.

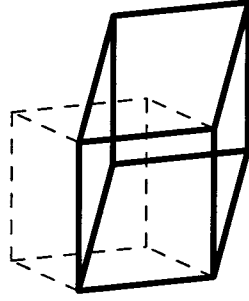


FIG. 3. Illustration of a cube distorted in the  $x$  and  $z$  directions by an amount  $\theta = 45^\circ$ .

**Example: Numerical dispersion for three-dimensional shear distortion.**

Let

$$(27) \quad \mathbf{k} = k[\cos(\phi) \sin(\Phi), \sin(\phi) \sin(\Phi), \cos(\Phi)]^t$$

be a wave vector as a function of the spherical angles  $\phi$  and  $\Phi$ . The exact phase velocity for (20)–(21) is given by  $\omega/k = c$  and the numerical phase velocity  $v = \tilde{\omega}/k$  is computed by specifying a value of  $\mathbf{k}$  as a function of  $\phi$   $\Phi$  and solving numerically for the value of  $\tilde{\omega}$  that satisfies (26).

In this example, a unit cube is sheared by an amount  $\theta$  in both the  $x$  direction and the  $z$  direction; see Figure 3.

In the computational experiments we take  $c = 1$  and  $\Delta t = 1/3$ . Figure 4 shows surfaces of the phase velocity error for shear angles of  $\theta = 0^\circ, 15^\circ, 30^\circ, 45^\circ$ . Each figure shows the velocity error for  $k = 1\pi/5$ , where the velocity error is defined as  $v - c$ . The shape of the velocity error surface remains the same as  $k$  is decreased, thus it is not necessary to display different surfaces. Note that the scale is different for each plot.

The maximum velocity, minimum velocity, and anisotropy ratio are tabulated in Table 2 as a function of  $k$  for each of the four grid distortions. The results demonstrate that, as the grid becomes more distorted, the numerical dispersion relation becomes more anisotropic.

It is possible to determine the rate of convergence of the numerical dispersion relation for distorted hexahedral grids by applying a least-squares fit to the above data. The logarithm of the error versus the logarithm of  $k$  is shown in Figure 5 for each of the four grids, along with a least-squares linear fit. The least-squares fit is applied to the maximum velocity error. For each grid the slope of the linear fit is approximately 2 (from 2.02 to 2.09), indicating second order convergence of the numerical dispersion relation.

**6. Linear system solution methods.** The VFETD method requires the solution of a large, sparse, symmetric, positive-definite mass matrix equation  $Cx = y$  at every time step. In this paper, the incomplete Cholesky conjugate gradient (ICCG) method will be used to solve the mass matrix. Basically, the ICCG method is a preconditioned conjugate gradient method where the preconditioner is constructed by applying the Cholesky factorization algorithm to the mass matrix  $C$  and ignoring the nonzero fill-in [39]. This generates an incomplete Cholesky factorization  $\tilde{L}\tilde{L}^t$ , where  $\tilde{L}$  has the same sparsity pattern as the matrix  $C$ . For the special case of a Cartesian grid, the following result holds.

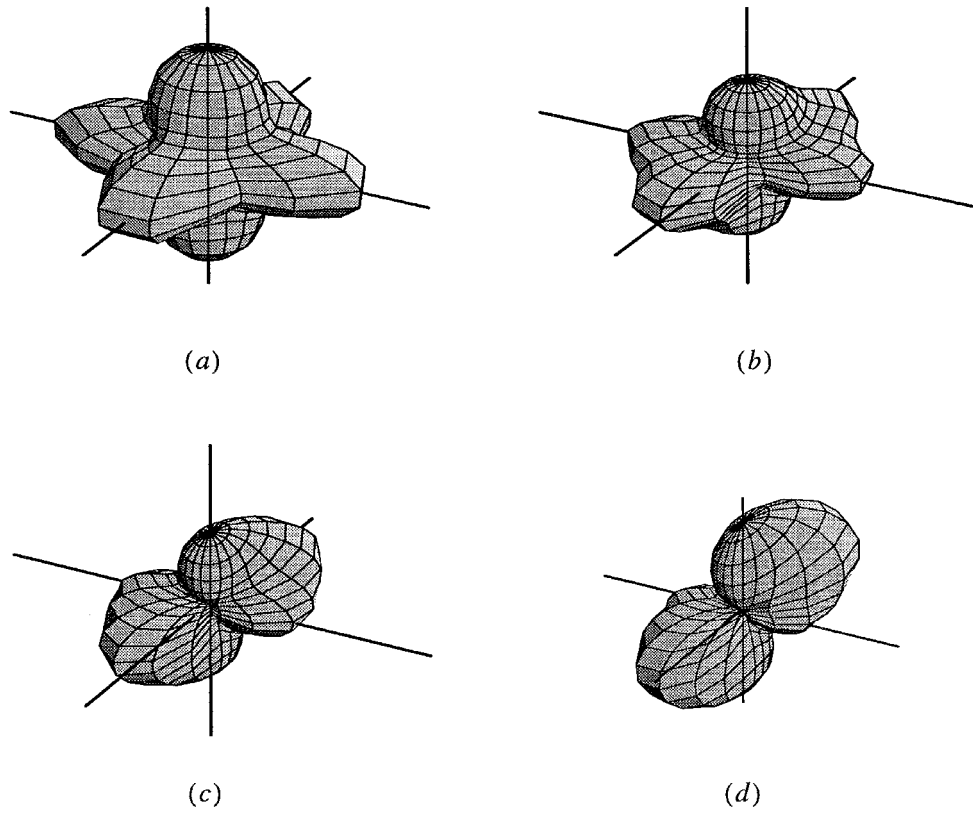


FIG. 4. Phase velocity error for  $\theta =$  (a)  $0^\circ$ , (b)  $15^\circ$ , (c)  $30^\circ$ , (d)  $45^\circ$ . The surface corresponds to  $k = 2\pi/5$ . The length of the axes are (a) 0.15, (b) 0.25, (c) 0.35, (d) 0.35.

TABLE 2  
Phase velocity and anisotropy ratio versus  $k$ .

| $\theta = 0^\circ$  |         |         |         | $\theta = 15^\circ$ |         |         |
|---------------------|---------|---------|---------|---------------------|---------|---------|
| $k$                 | max $v$ | min $v$ | ratio   | max $v$             | min $v$ | ratio   |
| $2\pi/5$            | 1.07538 | 1.03002 | 1.04404 | 1.08797             | 1.01709 | 1.06969 |
| $2\pi/10$           | 1.01845 | 1.00736 | 1.01101 | 1.02113             | 1.00423 | 1.01682 |
| $2\pi/15$           | 1.00816 | 1.00326 | 1.00488 | 1.00931             | 1.00188 | 1.00742 |
| $2\pi/20$           | 1.00458 | 1.00183 | 1.00274 | 1.00522             | 1.00106 | 1.00416 |
| $\theta = 30^\circ$ |         |         |         | $\theta = 45^\circ$ |         |         |
| $2\pi/5$            | 1.14536 | 1.00913 | 1.135   | 1.35058             | 1.00333 | 1.34609 |
| $2\pi/10$           | 1.03401 | 1.00227 | 1.0316  | 1.08656             | 1.00083 | 1.08566 |
| $2\pi/15$           | 1.01493 | 1.00101 | 1.0139  | 1.03845             | 1.00037 | 1.03807 |
| $2\pi/20$           | 1.00836 | 1.0057  | 1.00779 | 1.02163             | 1.00021 | 1.02142 |

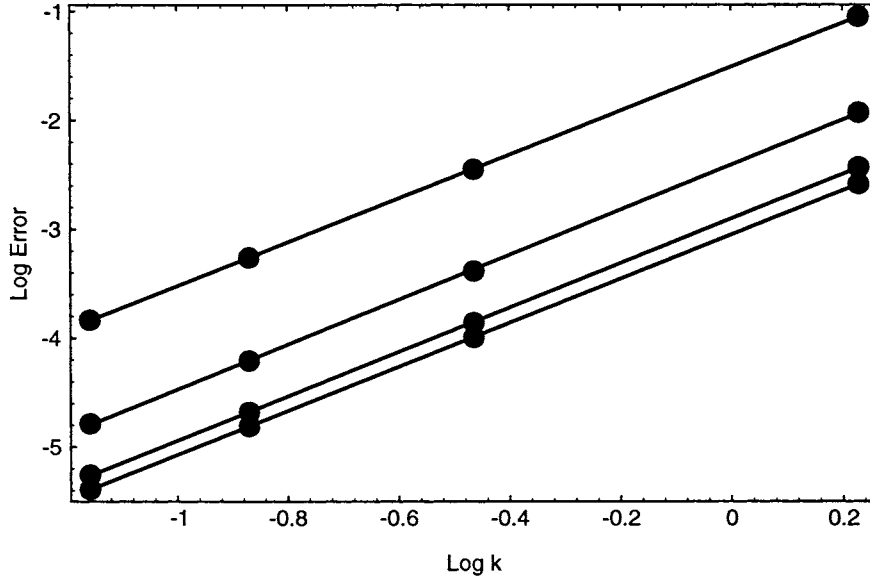


FIG. 5. Least-squares fit of phase velocity error indicating second order accuracy for distorted hexahedral grids with shear  $\theta = 0^\circ, 15^\circ, 30^\circ, 45^\circ$ , respectively. The larger error corresponds to the larger shear angle.

**THEOREM 4.** Consider the mass matrix  $C = [(\varepsilon \mathbf{W}_i, \mathbf{W}_j)]$  for an orthogonal hexahedral grid. Let  $C = LL^t$  be the Cholesky factorization and  $\tilde{L}\tilde{L}^t$  the incomplete factorization of  $C$ . Then  $L = \tilde{L}$ , i.e., there is no nonzero fill in the course of the Cholesky decomposition.

*Proof.* The proof follows by carefully examining the inner most loop of the decomposition (see Algorithm 4.2.2 in [39])

$$C_{ij} = C_{ij} - C_{ik}C_{jk},$$

where  $k < j \leq i$ . If  $C_{ij} = 0$ , i.e., there is no interaction between edges  $i$  and  $j$ , then there will be zero fill only if there is another edge  $k$  that interacts with both edges  $i$  and  $j$ . Numbering the edges sequentially precludes this possibility. This is illustrated on a two-dimensional grid in Figure 6.

It follows from the previous theorem that for the orthogonal case, the ICCG algorithm converges in one iteration. The above result does not hold for arbitrary hexahedral grids. However, as will be seen in the numerical results of the next section, the number of iterations for the ICCG algorithm to converge is quite small, indicating incomplete factorization is a very good preconditioner for the conjugate gradient algorithm.

The classical approach to dealing with the mass matrix is to “lump” it, whereby the matrix  $C$  is approximated by a diagonal matrix  $\tilde{C}$  given by

$$(28) \quad \tilde{C}_{ii} = \sum_j \alpha_j C_{ij}, \quad i = 1, \dots, N_e,$$

and the coefficients  $\alpha_j$  are such that

$$(29) \quad \sum_j \alpha_j \mathbf{W}_j \cdot \mathbf{W}_i = \int_{\Omega} \mathbf{E} \cdot \mathbf{W}_i d\Omega.$$

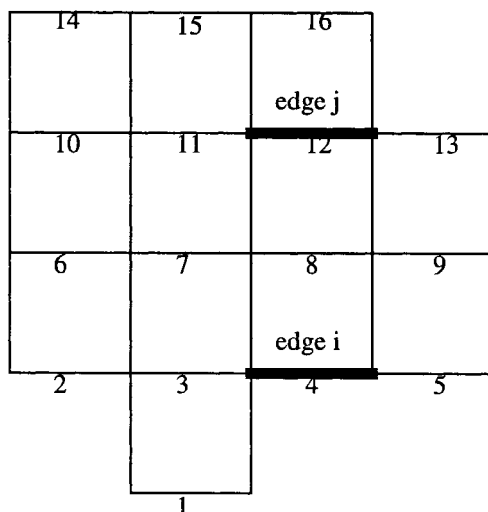


FIG. 6. Grid numbering scheme for Cartesian grid.

For a uniform orthogonal Cartesian grid and  $\alpha_j = 1$ , each diagonal term of the lumped mass matrix  $\tilde{C}$  is equal to the row-sum of  $C$  and the mass lumping approximation generates the classic FDTD method. Thus, we see that the VFETD method is a generalization of the FDTD method.

**7. Numerical experiments.** In this section the VFETD method is used to solve several electromagnetics problems for which analytic solutions are known. In all cases the CPU time is for a Silicon Graphics 8000 workstation (64 bit, 300 MFLOPS, SPECfp92 310).

**7.1. Spherical cavity.** In this section a perfectly conducting spherical cavity of radius  $a = 0.05855m$  is analyzed using VFETD and the computed solutions are compared to the exact analytical solution. The electric field within the cavity satisfies (20) where  $\sigma_E = \sigma_M = 0$  and  $\mu = \varepsilon = 1$  within the cavity. The exact solution is of the form

$$(30) \quad E = \sum_{np} A_{np} \mathbf{E}_{np}^{TE} \cos(\omega_{np} \mathbf{t} + \phi_{np}) + \sum_{np} B_{np} \mathbf{E}_{np}^{TM} \cos(\omega_{np} \mathbf{t} + \theta_{np}),$$

where the sum is over all the modes, and  $A$ ,  $B$ ,  $\phi$ , and  $\theta$  depend upon the initial conditions [37]. Here,  $\omega_{np}$  are the resonant frequencies given by

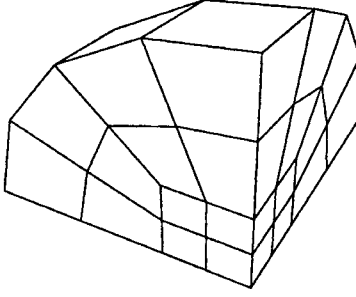
$$(31) \quad \omega_{np}^{(j)} = \frac{\zeta_{np}^{(j)}}{a}, \quad n, p = 1, 2, 3, \dots, j = 0, 1,$$

where  $\zeta_{np}^{(j)}$  are the  $p$ th zeros of the  $j$ th derivative of the spherical Bessel function of order  $n$ . The exact resonant frequencies below 20Hz are shown in Table 3.

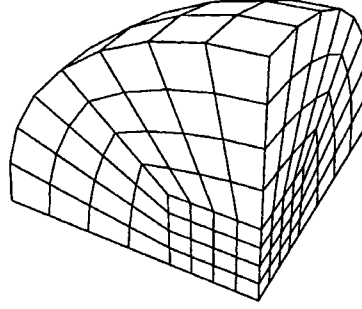
The spherical cavity was modeled using a sequence of hexahedral grids ranging from a coarse grid with 4 cells per radius to a fine grid with 12 cells per radius. Figure 7(a), (b) are cut-away views of the 256 hexahedral and 2048 hexahedral grids, respectively. The electromagnetic fields in the cavity were excited by a pulsed current source, the pulse having the shape of the second derivative of a Gaussian. The initial

TABLE 3  
Exact value of resonant frequencies below 20Hz.

| $\omega_{11}^{(1)}$ | $\omega_{21}^{(1)}$ | $\omega_{11}^{(0)}$ | $\omega_{31}^{(1)}$ | $\omega_{21}^{(0)}$ | $\omega_{41}^{(1)}$ | $\omega_{12}^{(1)}$ | $\omega_{31}^{(0)}$ |
|---------------------|---------------------|---------------------|---------------------|---------------------|---------------------|---------------------|---------------------|
| 7.4589              | 10.5665             | 12.2132             | 13.518              | 15.6654             | 16.4782             | 16.6277             | 18.9953             |



(a)



(b)

FIG. 7. Internal view of (a) 256, (b) 2048 hexahedral grid of sphere.

electric and magnetic fields within the cavity were zero. The simulation was run for  $t = 6.71315s$ , which corresponds to 50 periods of the lowest mode. An edge within the cavity was selected at random and the electric field along this edge was written to disk at every time step. This signal was weighted by a Hamming window and the signal was zero-extended to 32768 samples and then Fourier transformed. The magnitude of the Fourier transform is the *power spectrum* of the signal. The time step and the number of steps was different for each grid due to different stability requirements. The power spectrums for the 256 hexahedral case and the 2048 hexahedral case are shown in Figure 8(a), (b), respectively.

Naturally the power spectrum corresponding to the higher resolution grid is more accurate than the power spectrum corresponding to the lower resolution grid. The order of accuracy of the method is determined by performing a least-squares fit to the data where the error is defined to be the difference between the exact and computed values of  $\omega_{31}^{(1)}$ . In other words we assume that  $|(\omega_{31}^{(1)})_{exact} - (\omega_{31}^{(1)})_{computed}| \propto h^m$  and we solve for the value of  $m$  that best models the results. Table 4 records the error as a function of grid size, where  $h$  is the average cell size. The logarithm of the error versus the logarithm of  $h/a$  is shown in Figure 9, along with a linear least-squares fit. The slope of the line is 2.028, so that the method is second order accurate, thus agreeing with the numerical dispersion analysis.

The CPU time for the calculations is shown in Table 5. The CPU time is for the time stepping part of the calculation only. For the above experiments the matrix fill time is approximately 1/50 of the total CPU time. The stopping criteria for the ICCG algorithm was  $\|\mathbf{residual}\|_2 / \|\mathbf{rhs}\|_2 \leq 10^{-9}$ , where  $\mathbf{rhs}$  is the right-hand side. Note that the number of ICCG iterations does not increase as the grid is refined, indicating that the condition number of the mass matrix remains constant [38]. Therefore the computational cost per time step is proportional to the number of degrees of freedom.

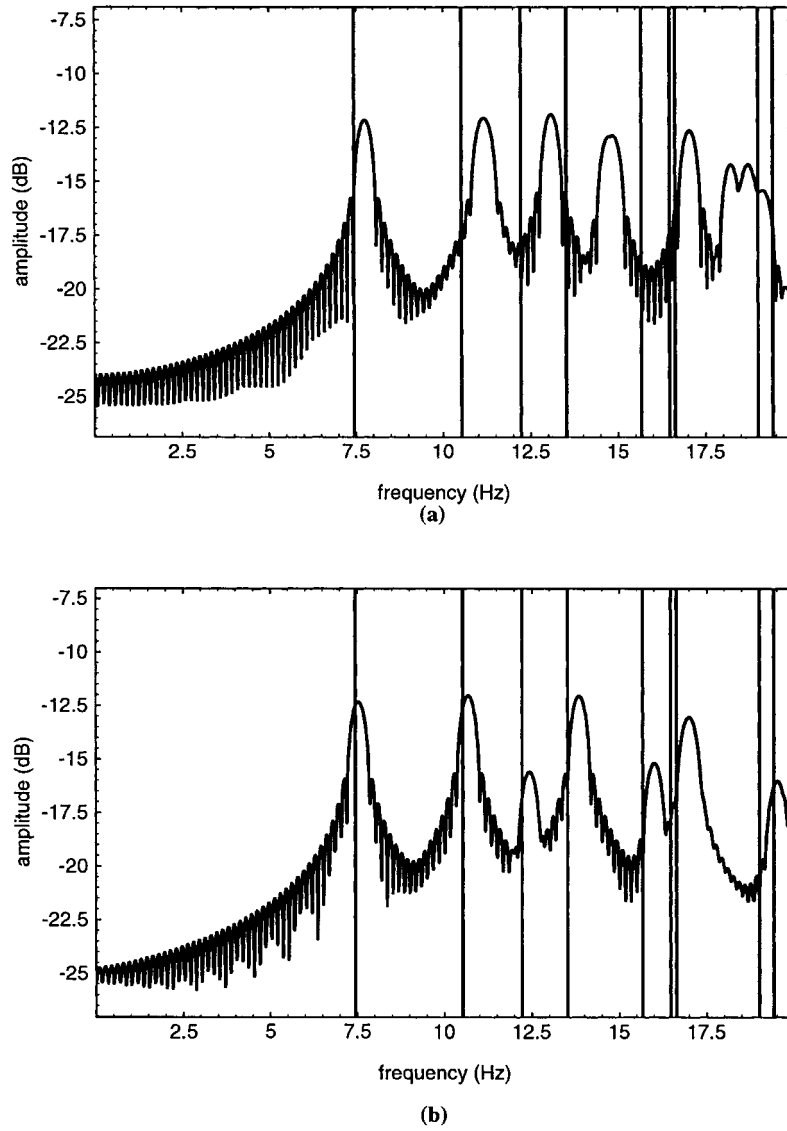


FIG. 8. Computed power spectrum versus exact for (a) 256, (b) 2048 hexahedral sphere.

TABLE 4  
Relative error of  $\omega_{31}^{(1)}$  resonant frequency versus grid size for hexahedral grid.

| $h/A$   | 1/4     | 1/6     | 1/8     | 1/10    | 1/12     |
|---------|---------|---------|---------|---------|----------|
| # nodes | 321     | 997     | 2273    | 4341    | 7393     |
| # cells | 256     | 864     | 2048    | 4000    | 6912     |
| # edges | 688     | 2400    | 5792    | 11440   | 19920    |
| error   | 0.09846 | 0.03960 | 0.02342 | 0.01589 | 0.009693 |



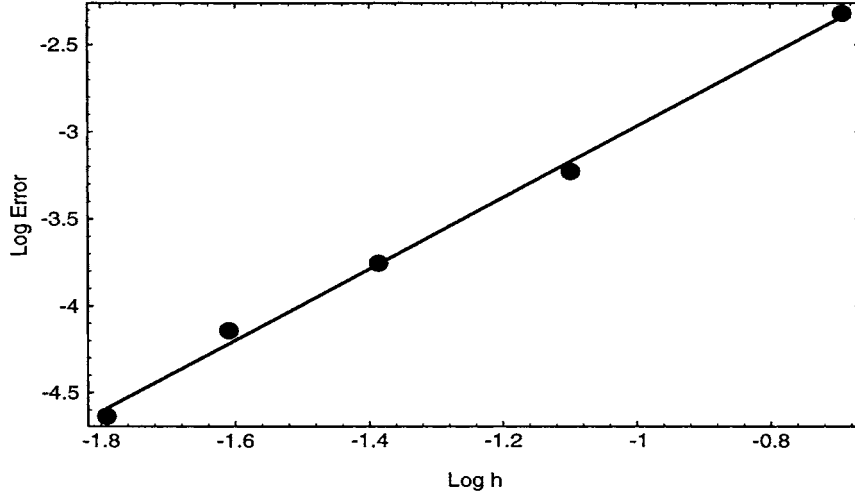


FIG. 9. Linear fit indicating second order accuracy.

TABLE 5

CPU time for cavity calculation versus grid size for hexahedral grid.

| # edges      | 688   | 2400 | 5792  | 11440 | 19920 |
|--------------|-------|------|-------|-------|-------|
| $\Delta t$   | .0035 | .002 | .0015 | .001  | .001  |
| # steps      | 1918  | 3356 | 4475  | 6713  | 6713  |
| # ICCG iter. | 7.8   | 7.8  | 7.8   | 7.8   | 7.8   |
| CPU sec.     | 107   | 731  | 3255  | 11962 | 22490 |

**7.2. Rectangular waveguide.** In this section, the VFETD method is used to compute the electromagnetic fields in a rectangular waveguide. Let the rectangular waveguide have width  $a = 0.9m$  in the  $x$  direction, height  $b = 4.5m$  in the  $y$  direction, and infinite in the  $z$  direction. The fields are modeled by (1)–(3).

A wave is launched by forcing the time dependent boundary condition

$$(32) \quad \begin{aligned} \mathbf{E}_x &= 0, \\ \mathbf{E}_y &= \left( 1 - \exp \left( - \left( \frac{t}{2T} \right)^2 \right) \right) \sin(\pi x/a) \sin(\omega t) \end{aligned}$$

at the left end ( $z = 0$ ) of the waveguide. Here  $\omega = 5.523599$  and  $T = 0.5$ . The initial electric and magnetic fields in the guide are zero. The exact steady state solution is given by

$$(33) \quad \begin{aligned} \mathbf{E}_x &= 0, \\ \mathbf{E}_y &= A \sin(\pi x/a) \sin(\omega t - \beta_z z), \\ \mathbf{E}_z &= 0, \end{aligned}$$

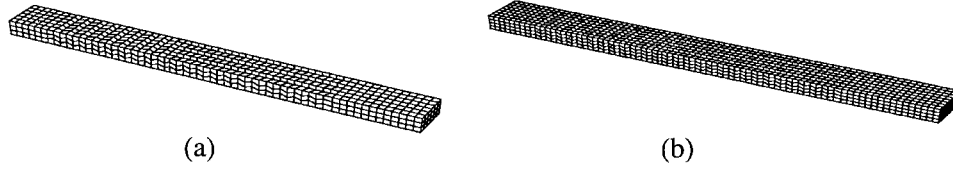


FIG. 10. Rectangular waveguide model using (a) 1080, (b) 2560 chevron cells.

$$\begin{aligned}
 \mathbf{B}_x &= \frac{\beta_z}{\omega} A \sin(\pi x/a) \sin(\omega t - \beta_z z), \\
 H_y &= 0, \\
 \mathbf{B}_z &= A \frac{(\pi/a)^2}{\omega} \cos(\pi x/a) \cos(\omega t - \beta_z z),
 \end{aligned}
 \tag{34}$$

where the wave number is  $\beta_z = \sqrt{\omega^2 \mu \varepsilon - (\pi/a)^2}$ ; see [36].

The waveguide is modeled using a sequence of chevron grids with the coarsest grid having  $h = a/6$  and the finest having  $h = a/14$ , where  $h$  is the average cell size. Several finite volume methods have been shown to be unconditionally unstable for these particular chevron grids [10]. Two of the grids are illustrated in Figure 10(a) and Figure 10(b).

The simulation was run for 20 seconds, which was enough time for the wavefront to propagate approximately 20 meters, i.e., twice the length of the finite guide.

The infinite waveguide is approximated by a finite length waveguide of length  $10m$  with a radiation (or absorbing) boundary condition. The method used here to eliminate nonphysical reflections from the artificial truncation of the domain is a variant of the perfectly matched layer (PML) method. The original PML method derived in [44] is applicable only for the classic Cartesian grid FDTD method, but many variants have been proposed for unstructured grids [45, 46, 47]. The general idea is to attach to the truncated domain several layers of anisotropic conductive media, using both electric and magnetic conductivity. Grading the layers from low conductivity to high conductivity creates a broadband impedance match, thus eliminating (or nearly eliminating) front face reflections. As the outgoing wave propagates through the PML it is absorbed by the medium. The PML is not really perfect; a small amount of energy will be reflected from the boundary. But the reflection is an exponential function of layer thickness and can be made arbitrarily small. Since the VFETD method allows for arbitrary tensor material properties, the PML technique was used without modification. In this example, the wave will be attenuated by the PML at the right end of the waveguide; thus the simulation will reach a dynamic steady state condition that resembles the exact solution of an infinite waveguide.

In this simulation, a five-layer PML was used to absorb the outgoing wave. Each layer is defined by the tensor material properties  $\mu$ ,  $\varepsilon$ ,  $\sigma_E$ ,  $\sigma_M$ . In every layer  $\mu$  and  $\varepsilon$  are identity matrices. The conductivity matrices are given by  $\sigma_E = \sigma_M = \sigma$ , where  $\sigma$  is a diagonal matrix with  $\sigma_{xx} = \sigma_{yy} = \sigma_{\perp}$  and  $\sigma_{zz} = 1$ . The values of  $\sigma_{\perp}$  used are tabulated in Table 6. The time step, number of steps, and ICCG iterations are shown in Table 7.

Note again that the number of ICCG iterations is constant. The same stopping criteria was the same as for the spherical cavity.

The computed electric and magnetic fields in the waveguide are compared to the

TABLE 6  
PML parameters used for truncated waveguide.

|                  | layer 1 | layer 2 | layer 3 | layer 4 | layer 5 |
|------------------|---------|---------|---------|---------|---------|
| $\sigma_{\perp}$ | 1.8     | 7.2     | 16.2    | 28.8    | 45      |

TABLE 7  
CPU time for chevron waveguide calculations.

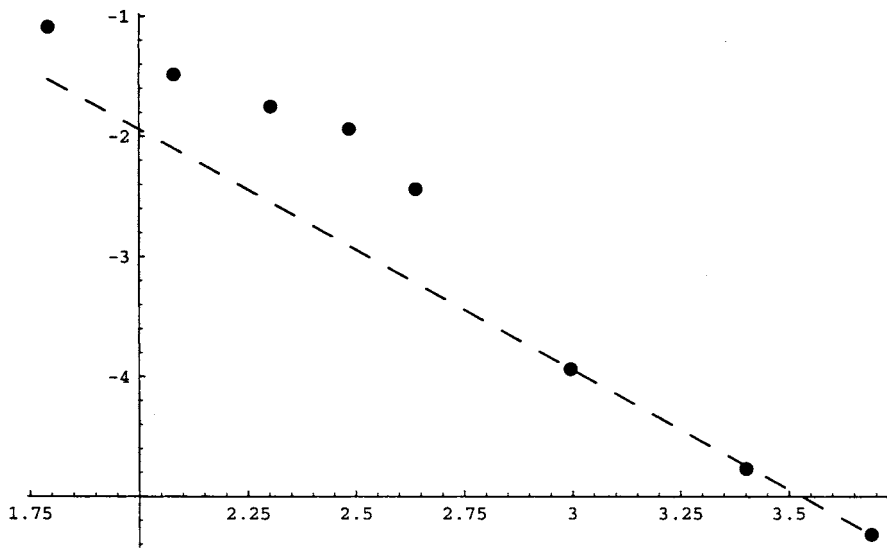
| $(h/a)$    | 1/6      | 1/8    | 1/10  | 1/14     | 1/20  | 1/40   |
|------------|----------|--------|-------|----------|-------|--------|
| # cells    | 1080     | 2560   | 5000  | 14720    | 35800 | 271200 |
| # edges    | 4425     | 9756   | 18215 | 47397    | 96469 | 771719 |
| $\Delta t$ | 0.016666 | 0.0125 | 0.01  | 0.007142 | .005  | .0025  |
| # steps    | 1272     | 1696   | 2120  | 2968     | 4240  | 8480   |
| ICCG iter. | 5.7      | 5.7    | 5.7   | 5.7      | 5.5   | 5.5    |

exact solution. The error measure is the standard  $L_2$  relative error shown below, where the sum is over all the hexahedral cells (excluding PML cells) in the grid.

$$(35) \quad L_2 \text{ error} = \frac{\|(\mathbf{E}_{\text{exact}} - \mathbf{E}_{\text{computed}})\|_2}{\|\mathbf{E}_{\text{exact}}\|_2}$$

The logarithm of the error versus the logarithm of  $(h/a)$  is shown in Figure 11. In this figure the initial error is somewhat erratic until the grid spacing  $h/a$  is approximately  $1/20$ , and after that the error decreases with second order convergence. This agrees with the analysis in [48] where it is shown that the Galerkin solution of the Helmholtz equation exhibits pollution due to numerical dispersion. In our example, the waveguide is ten wavelengths long and, for large values of  $h/a$ , the phase error builds up significantly along the length of the waveguide, degrading the  $L_2$ -norm of the error. As discussed in section 5, for a grid spacing of  $(h/a) = 10$  and a grid distortion of  $\theta = 30^\circ$  the worst-case phase velocity error is approximately 3%; therefore at the termination end of the waveguide the fields are up to 100 degrees out of phase, resulting in a local error of up to 50%. The  $L_2$  error for the  $(h/a) = 10$  case is 17.38%, which is relatively poor. The convergence result in Figure 11 shows that for electrically large problems a very fine mesh is required in order to achieve a small  $L_2$  error.

There are several other measures of error that are applicable for this specific waveguide problem. The global error as well as errors in impedance, wavelength, voltage standing wave ratio (VSWR), and reflection coefficient are shown in Table 8. In this case, the impedance in the guide is defined as  $Z = E_z/H_y = \omega\mu/\beta_z = \text{constant}$ . Since the computed fields are “noisy,” the computed impedance is defined to be the average impedance over the entire guide. The wavelength is computed by fitting a sine wave to the magnitude of the electric field, the period of best fit sine wave defining the wavelength of the electric field. The exact wavelength for this problem is simply  $\lambda_z = 2\pi/\beta_z$ . It is interesting to note that while the  $L_2$  error is relatively large, accurate quantities such as impedance and wavelength can be derived from the computed field. Hence the  $L_2$  error estimate may be overly pessimistic for some applications. The VSWR is defined as  $VSWR = |E_{\text{max}}|/|E_{\text{min}}|$ , where  $|E_{\text{max}}|$  is the maximum of the time average electric field in the waveguide and  $|E_{\text{min}}|$  is the minimum of the time

FIG. 11. *Log error versus Log h.*TABLE 8  
*Quality of computed fields for PML terminated waveguide.*

| $h/a$ | $L_2$  | impedance | wavelength | VSWR  | reflection coefficient |
|-------|--------|-----------|------------|-------|------------------------|
| 1/10  | 17.38% | 2.713%    | 0.453%     | 1.057 | -31dB                  |

average electric field in the waveguide. For an infinite waveguide, or a perfectly terminated finite length waveguide, the VSWR is 1.0. For a terminated waveguide, the VSWR can be expressed as a function of the reflection coefficient of the termination,  $VSWR = (1 - |\rho|)/(1 + |\rho|)$ , where  $\rho$  is the reflection coefficient. The VSWR was computed by determining the maximum and minimum fields over one period, and the reflection coefficient is then computed from  $|\rho| = (1 - VSWR)/(1 + VSWR)$ . The reflection coefficient is a measure of the effectiveness of the PML. If the PML is perfect, the reflection coefficient would be zero. The reported reflection coefficient of -31dB is comparable to that obtained when using finite difference methods on uniform grids [44]. The reflection coefficient can in theory be reduced arbitrarily by adding more layers and/or tuning the material properties. The computed electric and magnetic fields are shown in Figure 12 for the 5000 cell waveguide, with excellent qualitative agreement with theory. Note that the chevron pattern of the underlying computational grid is not imprinted on the computed fields.

**7.3. Dipole antenna.** In this section, we compute the radiated electromagnetic fields due to a small current source using the VFETD method. Starting at the origin, a current oscillating at frequency  $\omega$  is aligned in the  $z$  direction as illustrated in Figure 13.

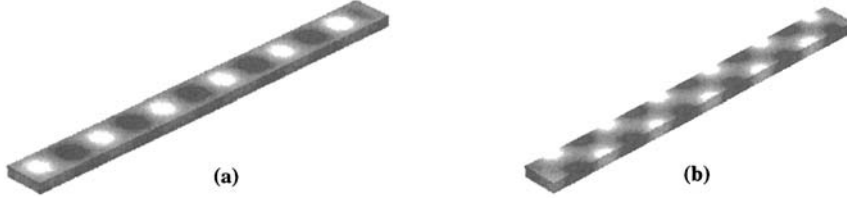
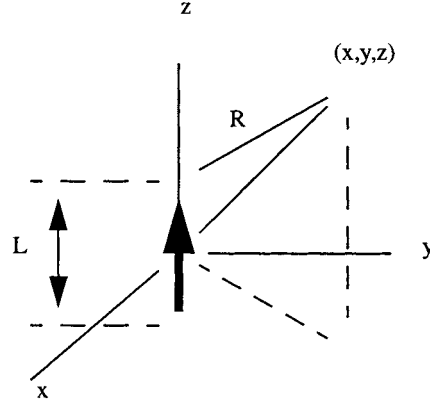
FIG. 12.  $z$ -component of (a) electric field (b) magnetic field in PML terminated waveguide.

FIG. 13. Coordinate system for dipole radiation calculation.

The exact solution is given by

$$(36) \quad \begin{aligned} \mathbf{B} &= \left( \mathbf{x} \frac{\partial A_z}{\partial y} - \mathbf{y} \frac{\partial A_z}{\partial x} \right) \cos(\omega t + \theta), \\ \mathbf{E} &= \frac{1}{\omega \mu \epsilon} \left( \mathbf{x} \frac{\partial^2 A_z}{\partial x \partial z} + \mathbf{y} \frac{\partial^2 A_z}{\partial y \partial z} - \mathbf{z} \left( \frac{\partial^2 A_z}{\partial x \partial x} + \frac{\partial^2 A_z}{\partial y \partial y} \right) \right) \sin(\omega t + \theta), \end{aligned}$$

where

$$(37) \quad A_z = \frac{\mu I}{4\pi} \int_{-L/2}^{L/2} \frac{\exp(-j\beta R)}{R} dz,$$

and  $\theta = \arg(A)$ . The parameters for this computational experiment were  $\omega = 107.3132$  and  $L = \lambda/12 = 0.00487916$ . The problem was modeled using a hemispherical grid consisting of 12032 hexahedral cells and 38005 edges. The grid had a spacing of  $h = \lambda/24 = 0.00243972$  at the origin with the grid spacing increasing away from the origin. The current source is exactly two edge lengths long and given by

$$(38) \quad I(t) = \left( 1 - \exp \left( - \left( \frac{t}{2T} \right)^2 \right) \right) \sin(\omega t),$$

where  $T = 0.0147$ . The simulation was executed for 0.05855 seconds using a time step of  $\Delta t = 10^{-4}$  seconds, which corresponds to 585 time steps.

In order to simulate free space, the same 5-layer PML used for the waveguide in the previous section was used with the exception that the conductivity tensor

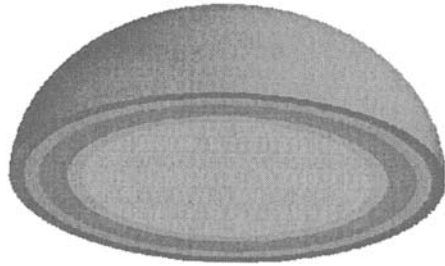


FIG. 14. Illustration of hexahedral grid with 5-layer PML used for dipole calculation.

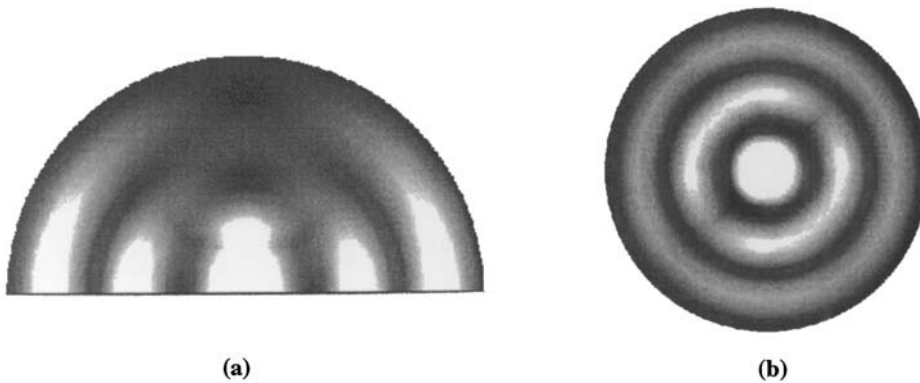


FIG. 15. Computed (a) electric (b) magnetic field magnitude in the vicinity of  $\lambda/12$  dipole.

is rotated such that the axial direction corresponds to the radial direction so that the PML will absorb outgoing waves. The PML begins at radius  $a = \lambda = 0.05855$  and the grid was terminated at  $b = 1.5\lambda = 0.087825$ ; see Figure 14. The global  $L_2$  error was computed in the same manner as for the waveguide, i.e., according to (35) where the sum is over all cells excluding PML cells. The computed electric field matched the exact electric field to within 1.6%, which is an excellent result since the electromagnetic field structure is quite complicated in the near field of the antenna. Snapshots of the computed electric and magnetic field are shown in Figure 15.

**8. Conclusion.** In this paper the VFETD method is derived, analyzed, and validated. It is demonstrated that the method is weakly stable, charge is conserved, and the continuity/discontinuity of the electromagnetic fields across a material interface are modeled properly. A numerical dispersion analysis indicates that the method is second order accurate, even on distorted, but regular, three-dimensional hexahedral grids.

However, like most finite element methods, the VFETD method requires that a sparse linear system be solved at every time step. The incomplete Cholesky conjugate gradient method was investigated where it is shown that the computational effort required to solve the system depends upon how distorted the grid is. However, for a uniformly refined mesh the number of iterations becomes independent of the number of mesh points; hence the method is scalable.

The VFETD method is validated by comparing computed solutions to analytical solutions for a simple resonant cavity, waveguide, and antenna. The accuracy and

computer CPU time is tabulated for a variety of different grids. The computational experiments performed on these distorted hexahedral grids have rates of convergence that agree with previously published analytical approximations. It is also shown that the recently developed PML concept can be used to approximate an infinite space using a finite grid. Since the VFETD method allows for arbitrary tensor material properties, the PML concept is trivial to implement.

**Acknowledgment.** The authors would like to thank the Institute for Scientific Computing Research (ISCR) at the Lawrence Livermore National Laboratory (LLNL) for their support in this research.

## REFERENCES

- [1] K. S. YEE, *Numerical solution of initial boundary value problems involving Maxwell's equations in isotropic media*, IEEE Trans. Antenna and Propagation, 14 (1966), pp. 302–307.
- [2] A. TAFLOVE AND M. E. BRODWIN, *Numerical solution of steady-state electromagnetic scattering problems using the time-dependent Maxwell's equations*, IEEE Trans. Microwave Theory Tech., 23 (1975), pp. 623–630.
- [3] A. TAFLOVE, *Review of the formulation and applications of the finite difference time domain method for numerical modeling of electromagnetic wave interactions with arbitrary structures*, Wave Motion, 10 (1988), pp. 547–582.
- [4] K. S. KUNZ AND R. J. LUEBBERS, *The Finite Difference Time Domain Method for Electromagnetics*, CRC Press, Boca Raton, FL, 1993.
- [5] R. HOLLAND, *The case against staircasing*, in Proceedings of the 6th annual Review of Progress in Applied Computational Electromagnetics, Monterey, CA, Applied Computation Electromagnetics Society, 1990, pp. 89–95.
- [6] N. MADSEN AND R. ZIOLKOWSKI, *A 3 dimensional modified finite volume technique for Maxwell's equations*, Electromagnetics, 10 (1990), pp. 147–161.
- [7] N. MADSEN, *Divergence preserving discrete surface integral method for Maxwell's curl equations using non-orthogonal unstructured grids*, J. Comput. Phys., 119 (1995), pp. 34–45.
- [8] R. HOLLAND, V. CABLE, AND L. WILSON, *Finite-volume time-domain techniques for EM scattering*, IEEE Trans. Electromagnetic Compatibility, 33 (1991), pp. 281–294.
- [9] K. S. YEE AND J. S. CHEN, *Conformal hybrid finite difference time domain and finite volume time domain*, IEEE Trans. Antennas and Propagation, 42 (1994), pp. 1450–1454.
- [10] S. BRANDON AND P. RAMBO, *Stability of the DSI electromagnetic update algorithm on a chevron grid*, in Proceedings of the 22nd IEEE International Conference on Plasma Science, Madison, WI, 1995.
- [11] D. J. RILEY AND C. D. TURNER, *VOLMAX: A solid model based transient volumetric Maxwell solver using hybrid grids*, IEEE Trans. Antennas and Propagation, 39 (1997), pp. 20–33.
- [12] V. SHANKAR, W. HALL, AND A. MOHAMMADIAN, *A time-domain differential solver for electromagnetic scattering problems*, Proc. IEEE, 77 (1989), pp. 709–721.
- [13] V. SHANKAR, A. MOHAMMADIAN, AND W. HALL, *A time-domain finite-volume treatment for the Maxwell equations*, Electromagnetics, 10 (1990), pp. 127–145.
- [14] R. W. NOACK AND D. A. ANDERSON, *Time-Domain Solutions of Maxwell's Equations Using a Finite-Volume Formulation*, AIAA paper 92-0451, 1992.
- [15] J. C. NEDELEC, *Mixed finite elements in  $R_3$* , Numer. Math., 35 (1980), pp. 315–341.
- [16] J. C. NEDELEC, *A new family of mixed finite elements in  $R_3$* , Numer. Math., 50 (1986), pp. 57–81.
- [17] A. BOSSAVIT, *Whitney forms: A class of finite elements for three-dimensional computations in electromagnetism*, Proc. IEE-A, 135 (1988), pp. 493–500.
- [18] A. BOSSAVIT AND I. MAYERGOYZ, *Edge elements for scattering problems*, IEEE Trans. Magnetics, 25 (1989), pp. 2816–2821.
- [19] J. LEE, D. K. SUN, AND Z. CENDES, *Tangential vector finite elements for electromagnetic field computation*, IEEE Trans. Magnetics, 27 (1991), pp. 4032–4035.
- [20] A. KONRAD, *Vector variational formulations of electromagnetic fields in anisotropic media*, IEEE Trans. Microwave Theory Tech., 24 (1976), pp. 533–559.
- [21] A. BOSSAVIT, *Solving Maxwell equations in a closed cavity, and the question of spurious modes*, IEEE Trans. Magnetics, 26 (1990), pp. 702–705.
- [22] Z. J. CENDES, *Vector finite elements for electromagnetic field calculations*, IEEE Trans. Magnetics, 27 (1991), pp. 3958–3966.

- [23] D. R. LYNCH, K. D. PAULSEN, AND W. E. BOYSE, *Synthesis of vector parasites in finite element Maxwell solutions*, IEEE Trans. Microwave Theory Tech., 41 (1998), pp. 1439–1447.
- [24] B. DILLON AND J. P. WEBB, *A comparison of formulations for the vector finite element analysis of waveguides*, IEEE Trans. Microwave Theory Tech., 42 (1994), pp. 308–316.
- [25] D. SUN, J. MAGNES, X. YUAN, AND Z. CENDES, *Spurious modes in finite element methods*, IEEE Antennas and Propagation, 37 (1995), pp. 12–24.
- [26] J. LEE, D. SUN, AND Z. CENDES, *Full-wave analysis of dielectric waveguides using tangential vector finite elements*, IEEE Trans. Microwave Theory Tech., 39 (1991), pp. 1262–1271.
- [27] B. ANDERSON AND Z. CENDES, *Solution of ferrite loaded waveguide using vector finite elements*, IEEE Trans. Magnetics, 31 (1995), pp. 1578–1581.
- [28] B. CRAIN AND A. PETERSON, *Analysis of propagation on open microstrip lines using mixed-order covariant projection vector finite elements*, Int. J. Microwave and Millimeter-Wave CAD, 5 (1995), pp. 59–67.
- [29] K. MAHADEVAN AND R. MITTRA, *Radar cross section computation of inhomogeneous scatterers using edge based finite element method in time and frequency domains*, Radio Science, 28 (1993), pp. 1181–1193.
- [30] K. MAHADEVAN, R. MITTRA, AND P. M. VAIDYA, *Use of Whitney's edge and face elements for efficient finite element time domain solution of Maxwell's equations*, J. Electromagn. Waves Appl., 8 (1994), pp. 1173–1191.
- [31] J. F. LEE AND Z. S. SACKS, *Whitney element time domain methods*, IEEE Trans. Magnetics, 31 (1995), pp. 1325–1329.
- [32] J. F. LEE, R. LEE, AND A. CANGELLARIS, *Time domain finite element methods*, IEEE Trans. Antennas and Propagation, 45 (1997), pp. 430–442.
- [33] J. LEE, *WETD—A finite element time domain approach for solving Maxwell's equations*, IEEE Microwave Guided Wave Letters, 4 (1994), pp. 11–13.
- [34] P. B. MONK, *A mixed method for approximating Maxwell's equations*, SIAM J. Numer. Anal., 28 (1991), pp. 1610–1634.
- [35] P. B. MONK, *Analysis of a finite element method for Maxwell's equations*, SIAM J. Numer. Anal., 29 (1992), pp. 714–729.
- [36] C. BALANIS, *Advanced Engineering Electromagnetics*, John Wiley and Sons, New York, 1989.
- [37] J. D. STRATTON, *Electromagnetic Theory*, McGraw–Hill, New York, 1941.
- [38] G. STRANG AND G. FIX, *An Analysis of the Finite Element Method*, Prentice–Hall, Englewood Cliffs, NJ, 1973.
- [39] G. H. GOLUB AND C. F. VAN LOAN, *Matrix Computations*, Johns Hopkins University Press, Baltimore, MD, 1989.
- [40] P. B. MONK AND A. K. PARROT, *A dispersion analysis of finite element methods for Maxwell's equations*, SIAM J. Sci. Comput., 15 (1994), pp. 916–937.
- [41] G. WARREN AND W. SCOTT, *Numerical dispersion in the finite elements method using triangular edge elements*, Microwave Optical Tech. Letters, 9 (1995), pp. 315–319.
- [42] D. WHITE AND G. RODRIGUE, *Improved vector FEM solutions of Maxwell's equations using grid pre-conditioning*, Internat. J. Numer. Methods Engrg., 40 (1999), pp. 3815–3837.
- [43] G. WARREN AND W. SCOTT, *An investigation of numerical dispersion in the vector finite element method using quadrilateral elements*, IEEE Trans. Antennas and Propagation, 42 (1994), pp. 1502–1508.
- [44] J. BERENGER, *A perfectly matched layer for the absorption of electromagnetic waves*, J. Comput. Phys., 114 (1994), pp. 185–200.
- [45] U. PEKEL AND R. MITTRA, *A finite element method frequency domain application of the PML concept*, Microwave and Optical Tech. Letters, 9 (1995), pp. 117–122.
- [46] Z. SACKS, D. KINGSLAND, R. LEE, AND J. LEE, *A perfectly matched anisotropic absorber for use as an absorbing boundary condition*, IEEE Trans. Antennas and Propagation, 43 (1995), pp. 1460–1463.
- [47] M. KUZUOGLU AND R. MITTRA, *Mesh truncation by perfectly matched anisotropic absorbers in the finite element method*, Microwave and Optical Tech. Letters, 12 (1996), pp. 136–140.
- [48] F. IHLENBURG AND I. BABUSKA, *Dispersion analysis and error estimation of Galerkin finite element methods for the Helmholtz equation*, Internat. J. Numer. Methods Engrg., 38 (1995), pp. 3745–3774.